*J Mater Sci: Mater Electron* **(2026) 37:1789**

# Dielectric relaxation and electrical transport mechanism of $NiFe_2O_4/MnPr_xFe_{2-x}O_4$ ($x \leq 0.10$) nanocomposites

M. A. Almessiere[1,2], A. Baykal[3,*], B. Ünal[4], Y. Slimani[1], and A. Demir Korkmaz[5]

[1] *Department of Biophysics, Institute for Research and Medical Consultations (IRMC), Imam Abdulrahman Bin Faisal University, P.O. Box 1982, 31441 Dammam, Saudi Arabia*
[2] *Department of Physics, College of Science, Imam Abdulrahman Bin Faisal University, P.O. Box 1982, 31441 Dammam, Saudi Arabia*
[3] *Food Engineering Department, Faculty of Engineering, Istanbul Aydin University, Florya, 34295 Istanbul, Turkey*
[4] *Department of Electrical and Electronics Engineering, Faculty of Engineering and Architecture, Istanbul Gelisim University, Avcılar, Istanbul, Turkey*
[5] *Department of Chemistry, Istanbul Medeniyet University, Uskudar, 34700 Istanbul, Turkey*

**Received:** 9 June 2026
**Accepted:** 3 August 2026
**Published online:** 10 August 2026

© The Author(s), under exclusive licence to Springer Science+Business Media, LLC, part of Springer Nature, 2026

## ABSTRACT

In this study, the dielectric relaxation and electrical transport mechanism of $MnPr_xFe_{2-x}O_4/NiFe_2O_4$ ($x \leq 0.10$) nanocomposites (NFO/$MnPr_xFe_{2-x}O_4$ ($x \leq 0.10$ NCs)) were systematically investigated as a function of the Praseodymium (Pr) substitution ratio ($x \leq 0.10$) and *temperature* (20–120 °C). MFO nanoparticles (NPs), NFO NPs, and NFO/$MnPr_xFe_{2-x}O_4$ ($x \leq 0.10$) NCs were created via a one-pot sol–gel route. XRD (X-ray powder diffraction) analyses confirmed the purity of MFO NPs, NFO NPs, and NFO/$MnPr_xFe_{2-x}O_4$ ($x \leq 0.10$) NCs (with the presence minor amount of $\alpha$-$Fe_2O_3$ for $x = 0.08$ and 0.1). The $D_{XRD}$ (crystallite size) of NCs was estimated between 24 and 57 nm. The characterization was performed using impedance spectroscopy and the electric modulus formalism to deconvolve the contributions from grain and grain boundary effects. All NCs exhibited semiconductor-like behavior with a negative temperature coefficient of resistance (NTCR), governed by a thermally activated hopping mechanism. A non-monotonic dependence of *dc* resistance on the substitution ratio was observed, with a minimum value, corresponding to maximum conductivity, identified at $x = 0.06$. Conversely, electric modulus analysis revealed that the bulk (grain) dielectric structure becomes maximally complex at $x = 0.04$, characterized by the emergence of multiple, well-resolved relaxation mechanisms. This differential influence of the dopant on the grain and grain boundary properties highlights a pathway for selectively engineering the overall conductivity and internal dielectric response of ferrite-based nanostructures for targeted electronic applications.

Address correspondence to E-mail: abdulhadibaykal@aydin.edu.tr

https://doi.org/10.1007/s10854-026-18201-z

## 1 Introduction

Due to their unique physicochemical properties (thermal, mechanical, optical, electrical, and magnetic properties such as low coercivity, high saturation magnetization, high Curie *T*, low anisotropy, high permeability, low magnetostriction, high electrical resistivity, etc.) and wide-ranging applications (photoluminescence, magnetic recording, biosensors, catalysis, humidity-sensors, magnetic refrigeration, photocatalysis, magnetic drug delivery, supercapacitors, permanent magnets, magnetic (hyperthermia), batteries including lithium-ion types, hyperthermia, etc.), spinel crystal structure is presented by $AB_2O_4$ formula in which A and B represent different metal cations. The A cation occupies A-site (tetrahedral, Td), while B cation resides in the B-site (octahedral, Oh) position, respectively. The type, placement, and quantity of these metal cations significantly affect the intrinsic chemical/physical properties of host SFNPs [1–3].

Apart from SFNPs, magnetic H/S NCs are also important materials due to their potential applications in microactuators, sensors, spins of electron devices apply in read heads, micromotors, etc. [4]. They have unique magnetization, microwave absorption, electromagnetic properties, and coercivity [5]. Rahman et al. studied both electroless deposition synthesis and exchange-spring of H/S $CoFe_2O_4/NiFe_2O_4$[6]. Feng et al. [7] applied hydrothermal route to prepare H/S $CoFe_2O_4/NiFe_2O_4$ core–shell structure. Slimani et al. [8] studied the impact of sonication time on the structural and magnetic characteristics of H/S $CoFe_2O_4/Ni_{0.8}Cu_{0.1}Zn_{0.1}Fe_2O_4$ NCs. Wang et al. investigated the exchange-coupling interaction in H/S $CoFe_2O_4/Fe_3O_4$ magnetic NCs [9]. The structural, magnetic, and hyperthermia properties of bimagnetic H/S and S/H ferrite NCs have been investigated by Jalili et al. [10], and they observed good exchange-coupling interaction between the hard and soft magnetic phases.

The main aims this study are to synthesize and examine the dielectric and electrical features of NFO/$MnPr_xFe_{2-x}O_4$ ($x \le 0.10$) NCs. The substitution of Pr into $MnFe_2O_4$ was varied in NFO/MFO NCs to understand its effect on the physical properties of the host.

## 2 Experimental

### 2.1 Chemicals and instrumentations

High-purity chemicals, $Ni(NO_3)_2.6H_2O$, $Mn(NO_3)_2{\cdot}6H_2O$, $Pr(NO_3)_3.6H_2O$ $Fe(NO_3)_3.9H_2O$, and citric acid, were received from Merck.

Rigaku Miniflex 600 X-ray diffractometer was used for the phase identification of products. SEM: Tescan Vega 3 Scanning Electron Microscope (SEM) along with EDX and Thermo Fisher Scientific Talos (TEM and HR-TEM) were used for the morphological and compositional analyses of NCs. Dielectric analyses were accomplished via the Novocontrol Alpha impedance analyzer.

### 2.2 Synthesis

The NFO/$MnPr_xFe_{2-x}O_4$ ($x \le 0.10$) NCs were produced using one-pot sol–gel route. First, a solution of NFO NPs was prepared by mixing the Ni and Fe nitrates salts in 80 ml of DI water by stirring at 90 °C for 45 min. (Beaker A). Second, stoichiometric quantities of Mn, Fe, and Pr nitrate salts (for $x = 0.0$ ratio, this precursor was not used) were dissolved in 80 mL DI water (Beaker B). Finally, solutions in beaker A and B solutions were mixed, and citric acid ($C_6H_8O_7$) was added to it. After that ammonia solution was used to fix the pH of final solution at 7, the *temperature* was set up at 160 °C for 50 min, and then at 310 °C to get black powder. Finally obtained solid product was calcinated 700 °C for 5 h [8, 11]. The same experimental procedure has been applied for all substitution ratios (x) (Scheme 1).

## 3 Results & discussion

### 3.1 Structure & morphology

The XRD powder patterns and unit cell representation of NFO/$MnPr_xFe_{2-x}O_4$ ($x \le 0.10$) NCs are given in Fig. 1. A single XRD pattern for all compositions (except for $x = 0.08$ and 0.1 NCs for which a tiny secondary phase of $\alpha$-$Fe_2O_3$, minor amount was observed) belongs to the cubic crystal lattice with the Fd3m space group. Miller indices (220), (311), (222), (400), (422), (511), (440), (620), and (533) were assigned for ICDD card #00-001-1121 ($MnFe_2O_4$). The

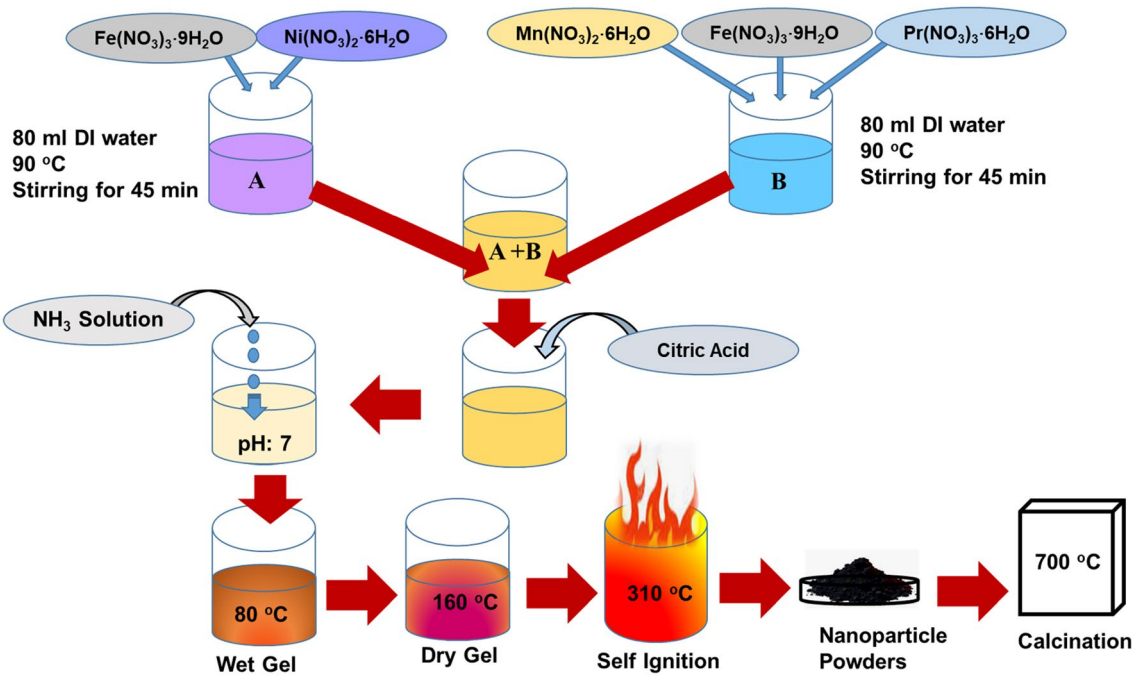


**Scheme 1** Flowchart for the one-pot sol–gel combustion synthesis of NFO/$MnPr_xFe_{2-x}O_4$ ($x \leq 0.10$) NCs

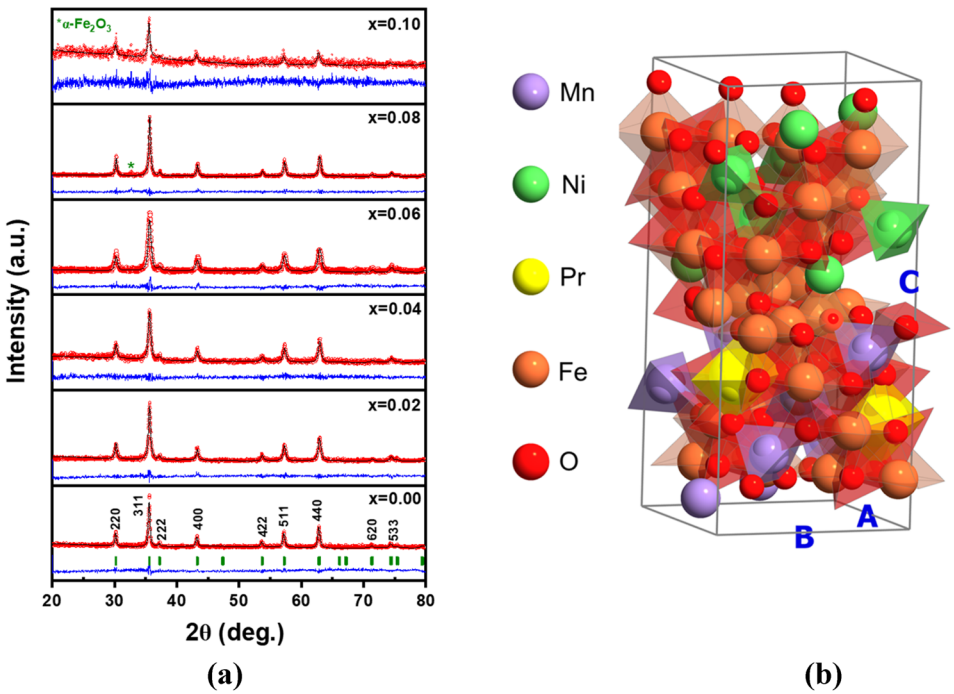


**Fig. 1** **a** XRD pattern and **b** unit cell representation of NFO/$MnPr_xFe_{2-x}O_4$ ($x \leq 0.10$) NCs

diffraction peaks are evidence of the indexed patterns of NFO and $MnFe_2O_4$. The structural and phase properties were analyzed using Match! 4 and FullProf software full-proof program according to the cards No. 01-086-2267 for $NiFe_2O_4$ and 01-074-2403 relevance to $MnFe_2O_4$, which employed Rietveld refinement of XRD data. Table 1 summarizes parameters including lattice constant ($a_0$), cell volume,

**Table 1** Refined structural parameters for NFO/$MnPr_xFe_{2-x}O_4$ ($x \leq 0.10$) NCs

| x | $a_o$ (Å) | V $(Å)^3$ | d $(g/cm^3)$ | $D_{XRD}$ (nm) | $R_{Bragg}$ | $\chi^2$ |
|---|---|---|---|---|---|---|
| 0.00 | 8.3645 | 585.21 | 5.235 | 54.5 | 34.2 | 1.4 |
| 0.02 | 8.3515 | 582.48 | 5.260 | 53.7 | 16.1 | 0.9 |
| 0.04 | 8.3466 | 581.46 | 5.269 | 27.2 | 20.1 | 0.8 |
| 0.06 | 8.3474 | 581.63 | 5.268 | 24.2 | 20.6 | 1.3 |
| 0.08 | 8.3483 | 581.81 | 5.266 | 57.7 | 10.0 | 0.9 |
| 0.10 | 8.3555 | 583.32 | 5.252 | 42.9 | 54.6 | 0.9 |

crystallite size, and XRD density. The lattice constant ($a_0$) did not exhibit a consistent trend as the Pr content increased, which is a result of atomic redistribution within the spinel lattice. The Debye–Scherrer equation was employed to determine the crystallite diameters, which were determined to be between 24 and 57 nm based on the (311) reflection [12]. SEM images were employed to investigate the surface morphology of NFO/$MnPr_xFe_{2-x}O_4$ ($x \leq 0.10$) NCs, as illustrated in Fig. 2. NPs were observed to exhibit dense agglomeration of primarily spherical particles in micrographs. The chemical composition of the synthesized NCs for $x = 0.02$ and 0.04 was analyzed using EDX, as illustrated in Fig. 3. The successful incorporation of all constituent elements was confirmed by the EDX spectra, which showed the presence of Ni, Mn, Pr, Fe, and O. TEM and HR-TEM analyses were employed to conduct additional structural and morphological validations for $x = 0.06$ NC (refer to Fig. 4). The particles' spherical nature was disclosed by TEM images, while HR-TEM images exhibited well-defined lattice fringes. The crystalline structure of the NCs was confirmed by the measurement of interplanar spacings using Gatan software.

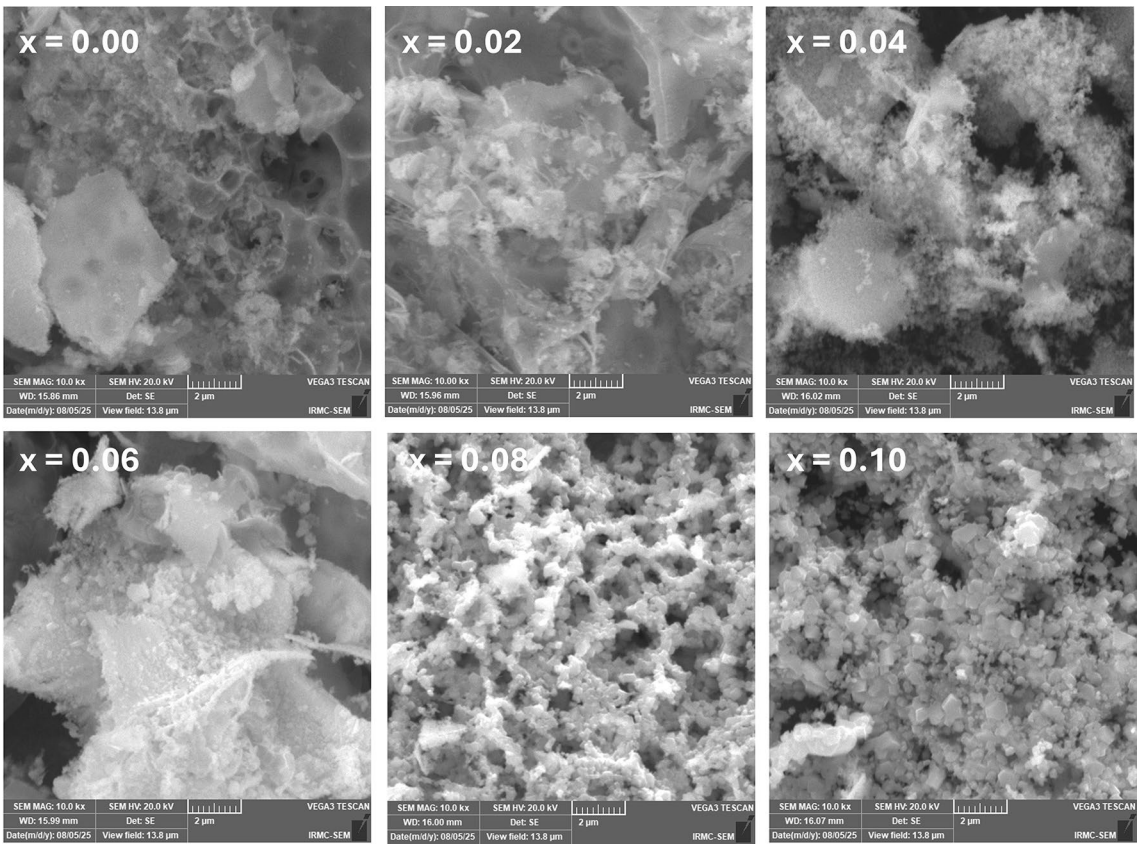


**Fig. 2** SEM images of NFO/$MnPr_xFe_{2-x}O_4$ ($x \leq 0.10$) NCs

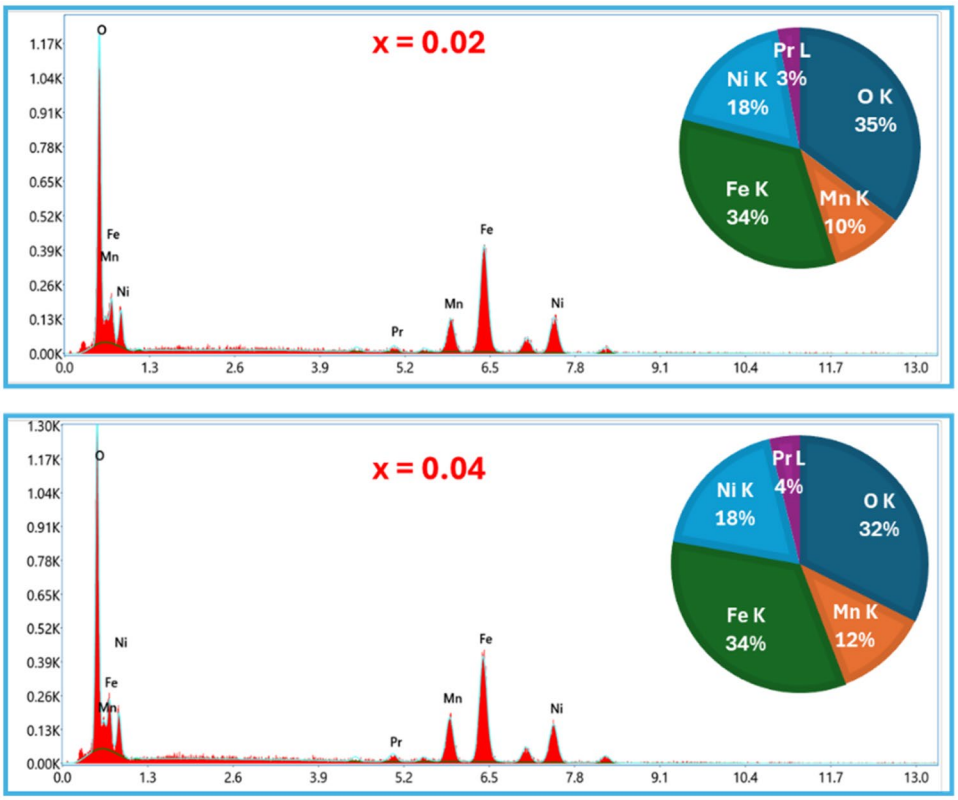


**Fig. 3** EDX spectra of NFO/$MnPr_xFe_{2-x}O_4$ ($x = 0.02$ and 0.04) NCs

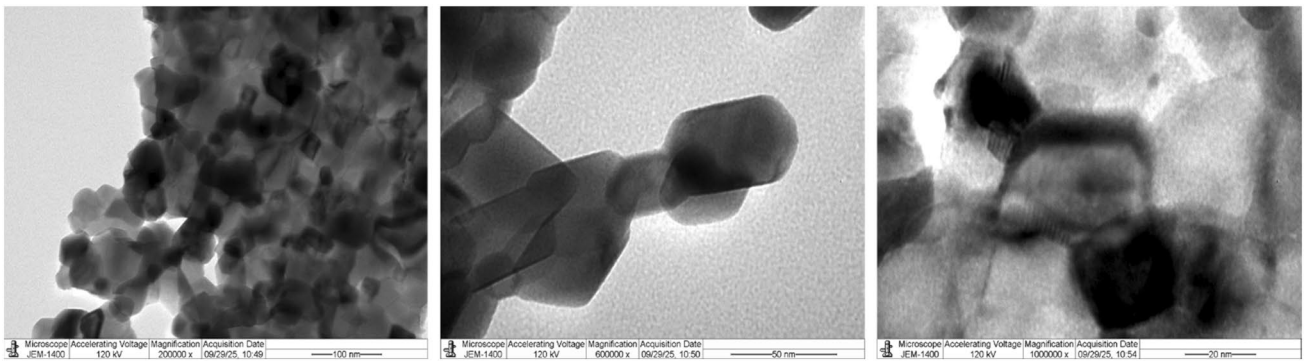

**Fig. 4** TEM and HR-TEM micrographs of NFO/$MnPr_xFe_{2-x}O_4$ ($x = 0.06$) NCs

## 3.2 Electrical & dielectric features

### 3.2.1 AC conductivity analysis

The *ac* conductivity ($\ln\sigma_{ac}$) behavior of NFO/$MnPr_xFe_{2-x}O_4$ ($x \leq 0.10$) NCs as shown in Fig. 5 was evaluated as a function of *temperature* (20–120 °C) and *frequency* (0–1 MHz). Careful investigation revealed that conductivity increased with increasing *temperature* and *frequency* in all NCs, thus confirming the thermally activated hopping conduction mechanism commonly observed in ferrites. Furthermore, while conductivity remained relatively constant at low *frequencies*, a significant increase was observed at high *frequencies*. This type of behavior is consistent with Jonscher's universal power law and is important in demonstrating the effectiveness of small polaron hopping (SPH) and connected barrier hopping (CBH) mechanisms [13]. While a smooth and stable conduction profile was obtained in the undoped ($x = 0.00$) NC, it is evident that medium-level Pr substitution (i.e., $x = 0.04$–$0.06$) exhibited more heterogeneous surface behavior due to structural disorder, lattice stress, and oxygen vacancies [13–15]. At higher substitution ratios (i.e., $x = 0.08$–$0.10$), it was determined that the

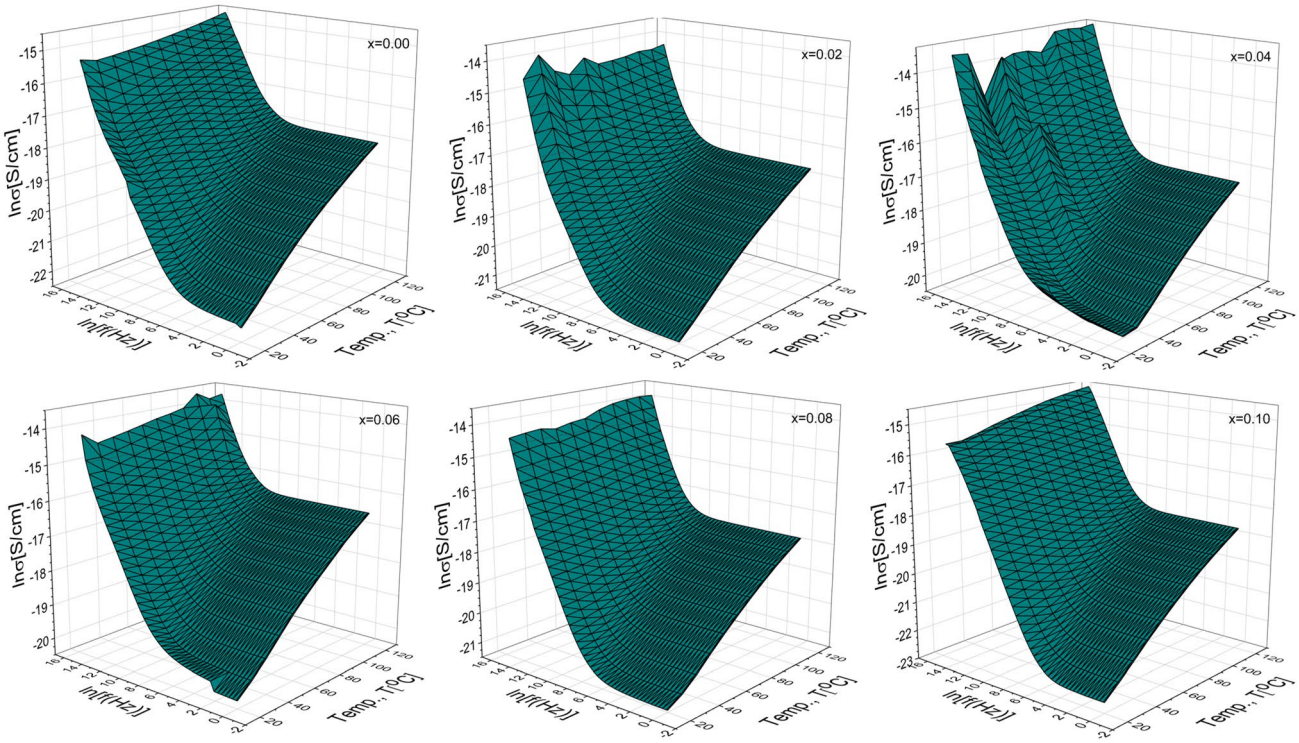


**Fig. 5** The *ac* conductivity of NFO/$MnPr_xFe_{2-x}O_4$ ($x \leq 0.10$) NCs

surfaces were re-smoothed and conductivity increased. This is associated with improved grain connections and defect reorganization. Moreover, the increase in conductivity with increasing *temperature* is of great importance as it supports Arrhenius-type thermal activation. In particular, the high conductivity observed in the $x = 0.10$ NC was considered indicative of a structural or electronic transition. The results reveal that $Pr^{3+}$ ion substitution affects the conduction mechanism in a nonlinear way and that appropriate substitution ratios can improve the electrical performance of ferrites [16].

### 3.2.2 DC conductivity and activation energy ($E_a$) analysis

The electrical conductivity in ferrite-based and other semiconducting ceramic materials typically exhibits thermally activated behavior, which can be described by the Arrhenius equation [6, 11]:

$$\sigma_{dc} = \sigma_0 \exp\left(-\frac{E_a}{k_B T}\right) \quad (1)$$

where $\sigma_{dc}$ stands for the *dc* electrical conductivity, $\sigma_0$ presents the pre-exponential factor (a *temperature*-independent constant), and $k_B$ is the Boltzmann constant. This relation implies that the $E_a$ can be extracted from the slope of the linear fit to a plot of $\ln(\sigma_{dc})$ versus $1/k_BT$.

The *dc* conductivity behavior of NFO/$MnPr_xFe_{2-x}O_4$ ($x \leq 0.10$) NCs depicted in Fig. 6 was investigated within the framework of the Arrhenius model [14], and the $\ln(\sigma_{dc})$–$1/k_BT$ graphs clearly showed a linear trend. As is known, this result confirms that electrical conduction is controlled by a single-dominant thermal activation mechanism. The increase in conductivity as *temperature* increases demonstrates with significant efficiency that charge carriers can overcome conduction barriers with the aid of thermal energy. Thus, it was determined that the $Pr^{3+}$ ion substitution has a nonlinear effect on conductivity. In particular, conductivity reaches its maximum level for $x = 0.04$ and 0.06 NCs, while it decreases again at higher substitution ratios. *Ea's* were calculated as 444, 425,375, 375, 433, and 422 meV, respectively, as listed in Table 2. The decrease in $E_a$ values up to $x = 0.06$ shows us that more favorable conduction paths for electron hopping are formed. This behavior is explained by electron hopping between $Fe^{2+}/Fe^{3+}$ ions, the alteration of cation distribution by $Pr^{3+}$ ion substitution ratio, and the construction of lattice stresses [16, 17]. At high substitution

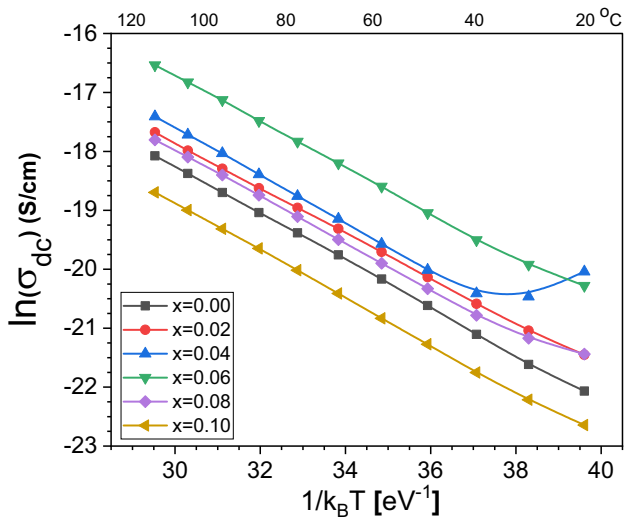


**Fig. 6** Arrhenius plot of the *dc* conductivity of NFO/$MnPr_xFe_{2-x}O_4$ ($x \leq 0.10$) NCs

ratios, the activation energy increased again due to excessive structural disorder, defect density, and grain boundary resistance. Therefore, the results show that optimum electrical performance is obtained in the range $x \approx 0.04$–$0.06$. Thus, this reveals that $Pr^{3+}$ ion substitution makes the electrical properties of ferrite systems tunable by affecting both the microstructure and charge carrier mobility. These results underscore the importance of compositional tuning in optimizing the electrical performance of spinel ferrites for *temperature* sensitive applications [18, 19].

### 3.3 Dielectric constant analysis

The dielectric behavior of NFO/$MnPr_xFe_{2-x}O_4$ ($x \leq 0.10$) NCs shown in Fig. 7 was evaluated by examining $\ln\varepsilon_r'$ as a function of *frequency* and *temperature*. It is important to note that the dielectric constant decreases with increasing *frequency* in all NCs. It is a well-known behavior that dipoles can follow the applied alternating electric field at low

**Table 2** *Ea*'s of Pr → MFO/NFO ($x \leq 0.10$) NCs

| $x$ | 0.00 | 0.02 | 0.04 | 0.06 | 0.08 | 0.10 |
|---|---|---|---|---|---|---|
| *Ea* (eV) | 0.444 | 0.425 | 0.375 | 0.375 | 0.433 | 0.422 |

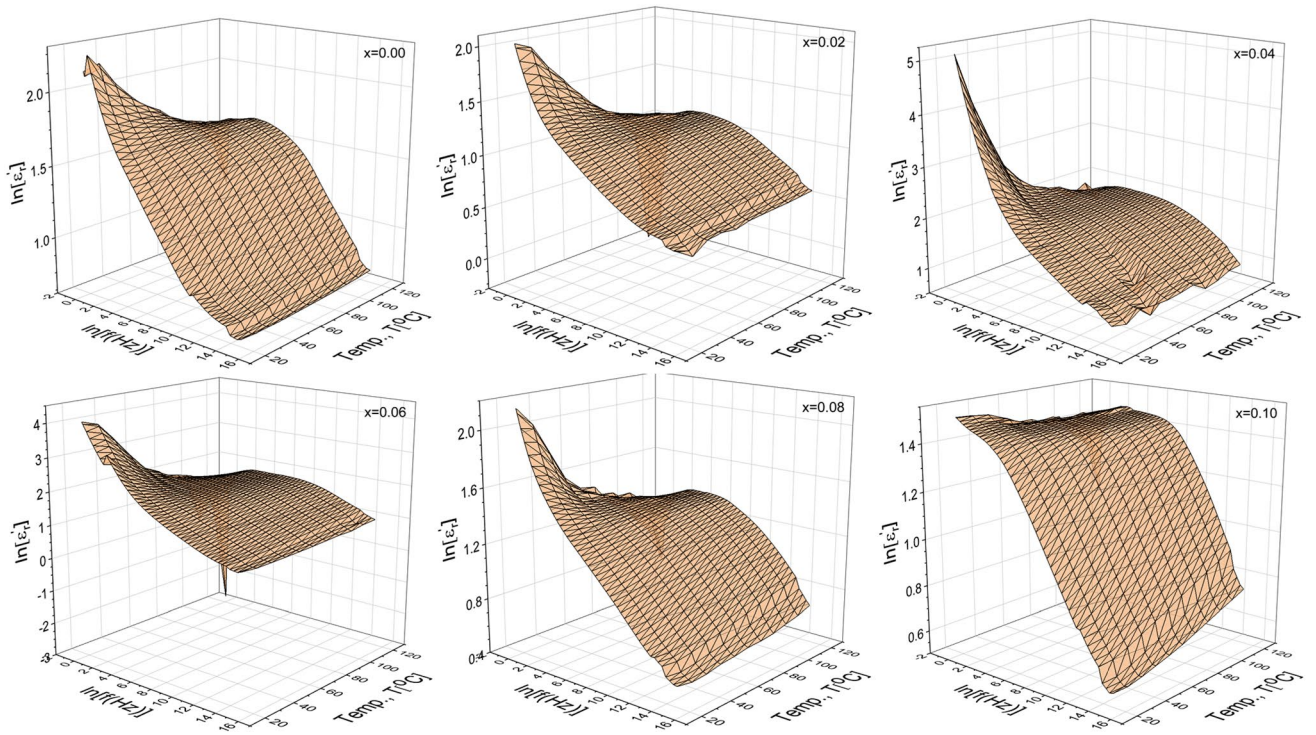


**Fig. 7** Dielectric constant of NFO/$MnPr_xFe_{2-x}O_4$ ($x \leq 0.10$) NCs

*frequencies* but exhibit classical dielectric dispersion at high *frequencies* due to the inability of this alignment to occur. The temperature effect was observed to vary depending on the substitution ratio. Therefore, while $\varepsilon_r$ remains relatively constant at low *temperatures*, it reaches a certain maximum value as the *temperature* increases and then exhibits plateau or decreasing behavior. This situation is explained by the fact that *temperature* increases dipole mobility and thermal disorder becomes dominant at high *temperatures*. A significant maximum was observed, particularly in the example $x = 0.04$; this was associated with dielectric relaxation or possible structural/magnetic phase transitions. At substitution levels of $x = 0.06$ and above, it was determined that the surfaces become smoother and the relaxation behavior weakens. The *frequency*-dependent decrease reveals the influence of electronic, ionic, directional, and interfacial polarization mechanisms. The results show that the $Pr^{3+}$ substitution significantly alters polarization processes, charge carrier mobility, and dielectric response. Therefore, it is concluded that composition optimization is critical for sensors, energy storage systems, and electronic applications [20].

### 3.4 Dielectric loss analysis

The dielectric loss ($\ln\varepsilon_r''$) behavior of NFO/$MnPr_xFe_{2-x}O_4$ ($x \le 0.10$) NCs as displayed in Fig. 8 was analyzed as a function of *temperature* and *frequency*. As can be seen in all NCs, the dielectric loss was observed to be high at low *frequencies* and decreased significantly as the *frequency* increased. Therefore, this situation is explained by the fact that energy loss increases at low *frequency* due to the ability of dipoles and charge carriers to follow the electric field, while these mechanisms become insufficient at high *frequencies*. It was observed that increasing *temperature* increased the dielectric loss, especially at low *frequencies*. The main reason for this is that *temperature* strengthens conductivity losses by increasing charge carrier mobility. While the classic high–low-*frequency* loss was observed in $x = 0.00$ and 0.02 NCs, it should be emphasized that differentiations in relaxation mechanisms emerged in $x = 0.04$ and 0.06 NCs. In addition, the general trend was preserved at higher substitution

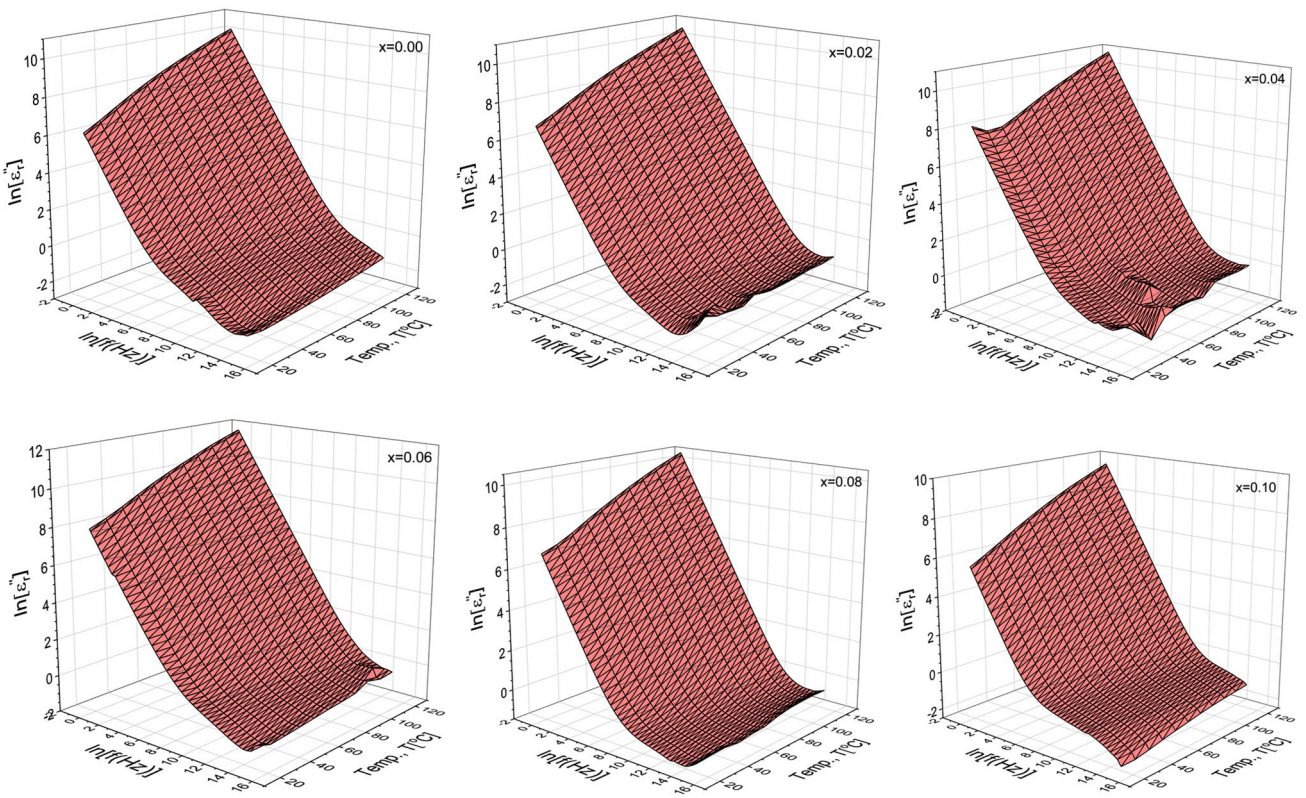


**Fig. 8** Dielectric loss of NFO/$MnPr_xFe_{2-x}O_4$ ($x \le 0.10$) NCs

ratios ($x = 0.08$–$0.10$), but the distribution of loss values changed. The results show that conductivity losses, dipole relaxation, and Maxwell–Wagner type interfacial polarization are effective in energy loss. Thus, it was determined that $Pr^{3+}$ ion substitution causes significant changes in oxygen vacancies, grain size, grain boundary properties, and charge carrier density. In other words, these changes make it possible to control the dielectric loss. While low loss values provide an advantage for high-*frequency* electronic applications, controlled energy loss is expected to be useful in applications such as electromagnetic absorbers and heating systems. In conclusion, it has been shown that Pr substitution expands the functional applications of ferrites by regulating energy loss mechanisms [16, 21].

### 3.5 Dissipation factor analysis

The detail dissipation factor behavior of NFO/$MnPr_xFe_{2-x}O_4$ ($x \leq 0.10$) NCs is shown in Fig. 9 as a function of *temperature* and *frequency* of ln(tan$\delta$). It was determined that the tan$\delta$ value increases with increasing *temperature* and decreases with increasing *frequency* in all NCs. Therefore, this trend reflects the dielectric relaxation behavior commonly observed in ferrites. As is well known, energy loss increases at low *frequencies* because dipoles and charge carriers can more easily follow the applied electric field. Conversely, at high *frequencies*, the dissipation factor decreases because the alignment of dipoles becomes more difficult. While a uniform distribution is observed in the undoped NC, fluctuations and distinct peaks indicating new relaxation processes appear, especially in substitution ratio of $x = 0.04$ and 0.06, with increasing Pr substitution ratio. That is, the strong peak observed in the $x = 0.06$ NC shows that lattice stress, changes in cation distribution, and defect formation increase energy loss. Furthermore, it was determined that these peaks broadened or weakened at higher substitution ratios. The results reveal that electron hopping ($Fe^{2+} \leftrightarrow Fe^{3+}$), ionic polarization, spatial charge polarization, and multiple relaxation times have an effect on the dissipation factor. It was understood that $Pr^{3+}$ ions disrupt the lattice structure due to their large ionic radius, construct oxygen vacancies, and alter the charge carrier behavior. These properties are important for electromagnetic

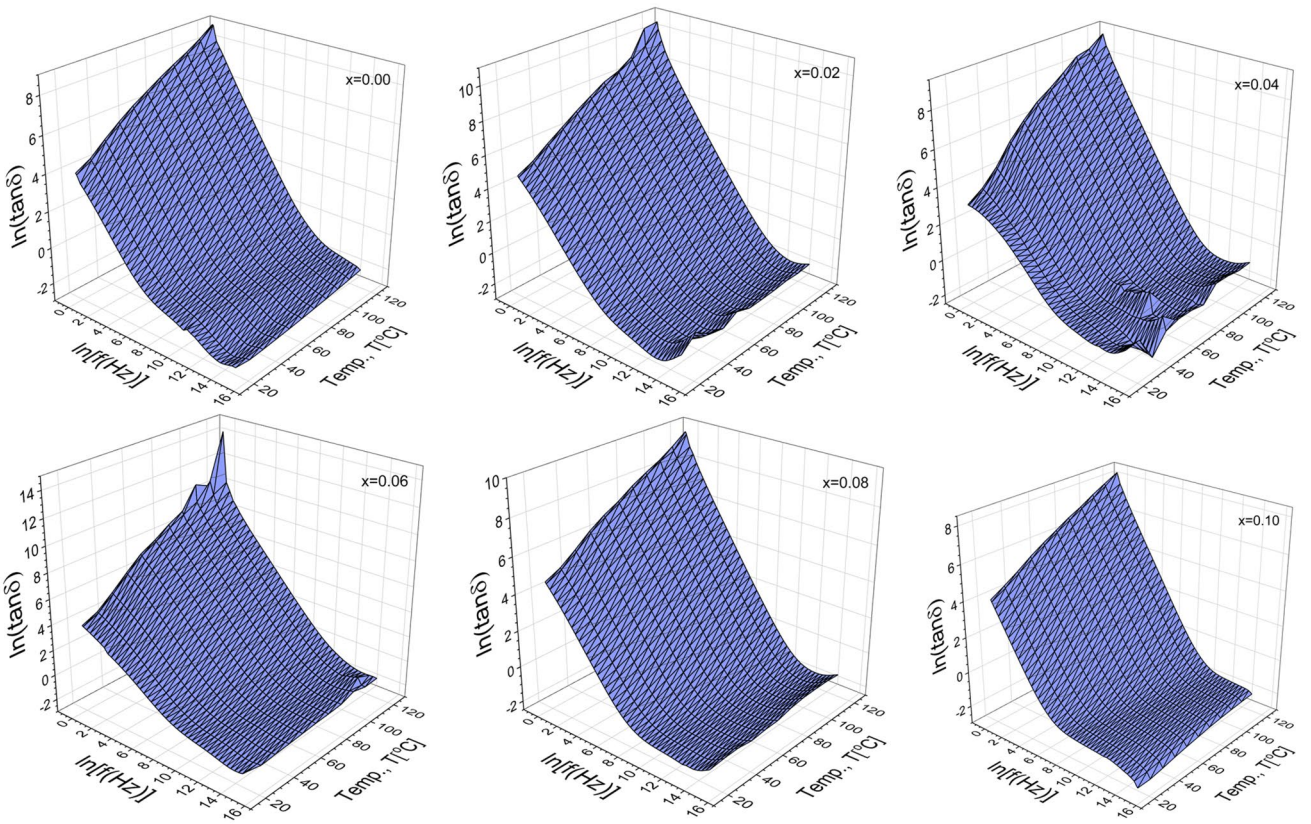


**Fig. 9** Dissipation factor of NFO/$MnPr_xFe_{2-x}O_4$ ($x \leq 0.10$) NCs

shielding, high-*frequency* electronics, and applications where energy loss needs to be controlled. In particular, the $x = 0.06$ NC showed remarkable performance due to the optimized relaxation processes [16, 20].

### 3.6 Real electrical modulus (ReM) analysis

The real electrical modulus (ReM) behavior of NFO/$MnPr_xFe_{2-x}O_4$ ($x \leq 0.10$) NCs is depicted in Fig. 10 as a function of *frequency* and *temperature*. It was observed that the ReM values remained high and constant at low *temperature*s, while they decreased rapidly and approached zero at high *temperature*s. Therefore, this behavior at low *temperature*s represents the "frozen" state where the charge carriers are immobile and the system exhibits capacitive character. Accordingly, as the *temperature* increases, the charge carrier mobility increases, and the system acquires a conductive character. Moreover, the sigmoidal transition observed in the mid-*temperature* region is indicative of thermally activated dielectric relaxation processes. Consequently, the shift of this transition region to higher *temperature*s as the *frequency* increases confirms the Arrhenius-type relaxation behavior. Although the shape of the ReM curves is similar in all NCs, the $Pr^{3+}$ ion substitution significantly altered the maximum ReM values. For example, in the case of $x = 0.02$, the maximum ReM increased to approximately 0.6, while at $x = 0.04$ it decreased to approximately 0.4. It has been stated that these changes are related to the high-*frequency* dielectric constant and that $Pr^{3+}$ ion substitution affects the charge carrier dynamics. The basic mechanism of electrical relaxation has been evaluated as $Fe^{2+} \leftrightarrow Fe^{3+}$ electron hopping and Maxwell–Wagner interface polarization [8]. Furthermore, it has been concluded that $Pr^{3+}$ ions cause lattice distortion due to their large ionic radius, altering the cation distribution and affecting the core–shell interface properties. The findings demonstrate that $Pr^{3+}$ ion substitution is an effective method for tuning the dielectric response of ferrite NPs.

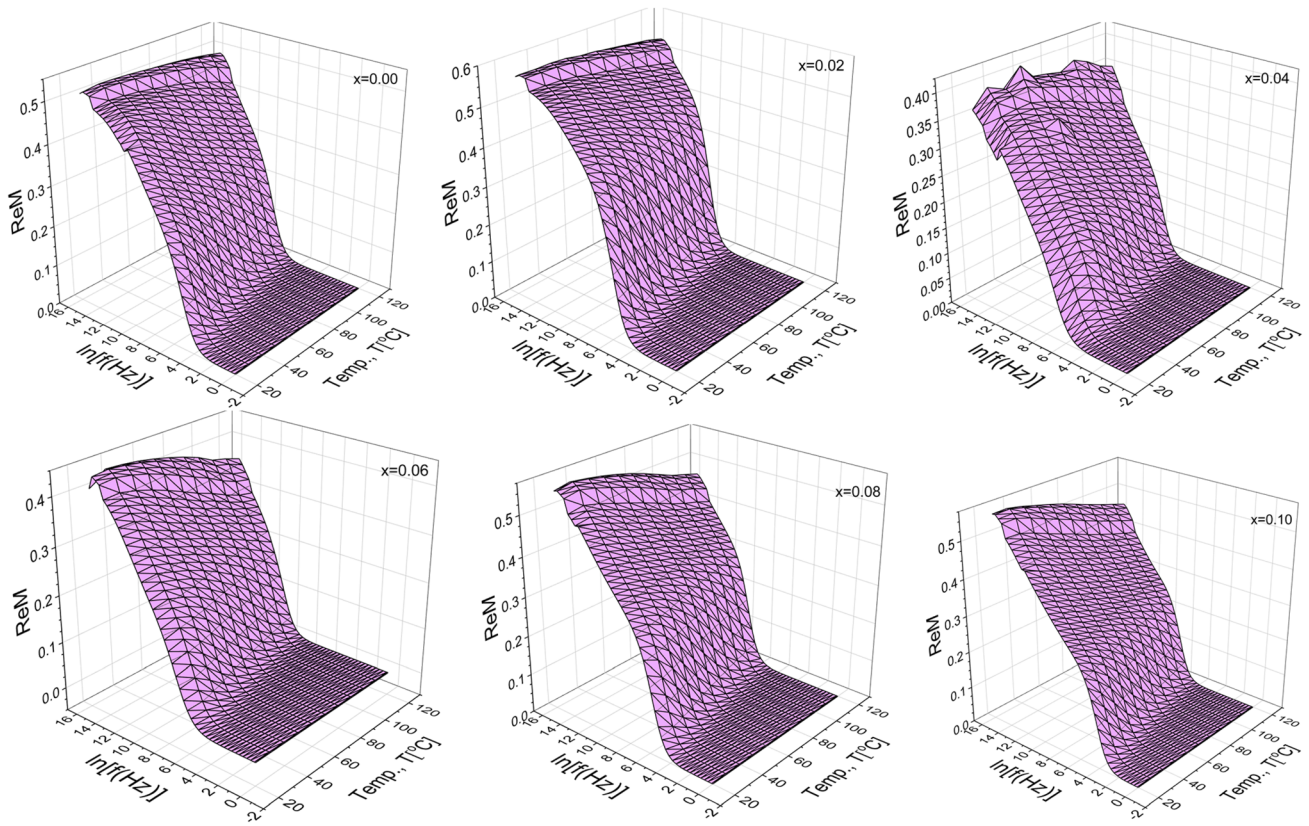


**Fig. 10** Real modulus of NFO/$MnPr_xFe_{2-x}O_4$ ($x \leq 0.10$) NCs

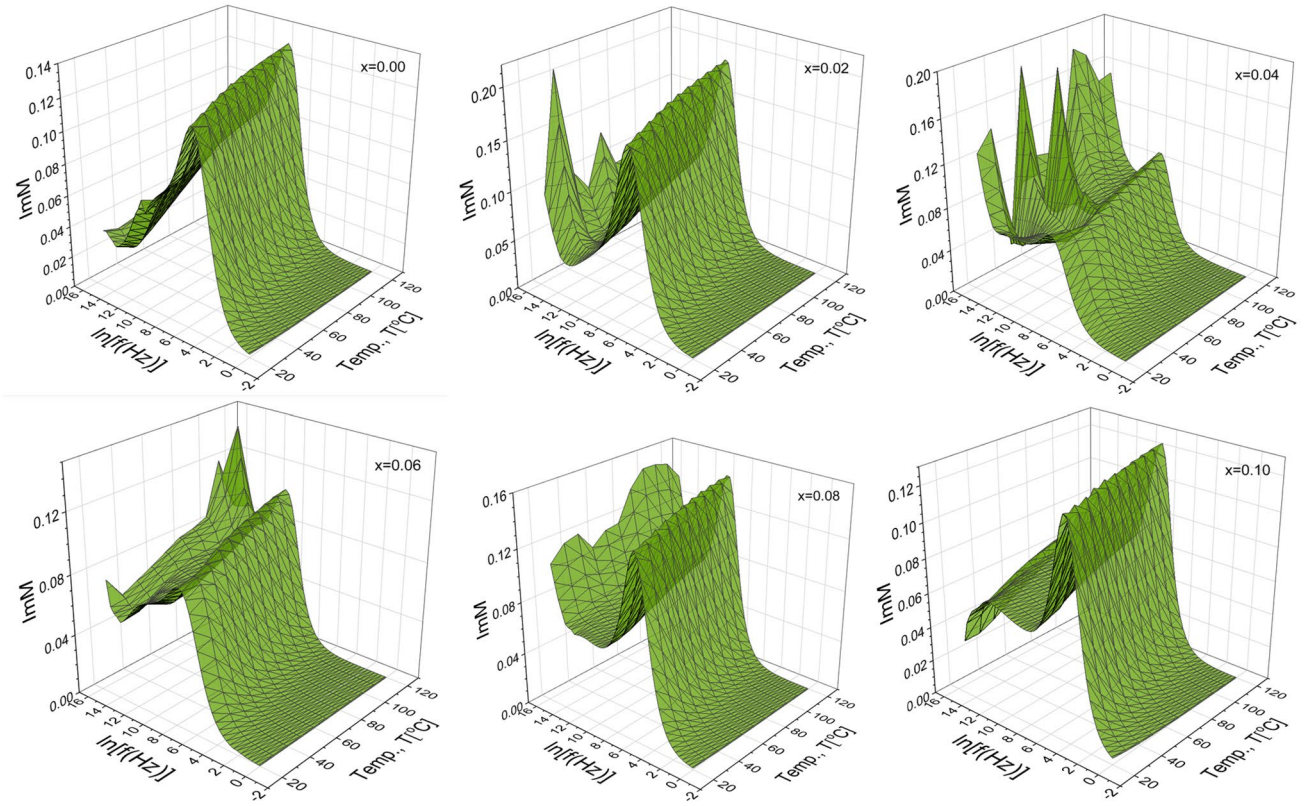


**Fig. 11** Imaginary modulus of NFO/$MnPr_xFe_{2-x}O_4$ ($x \leq 0.10$) NCs

## 3.7 Imaginary modulus (ImM) analysis

The imaginary electric modulus (ImM) behavior of NFO/$MnPr_xFe_{2-x}O_4$ ($x \leq 0.10$) NCs is presented in Fig. 11 as a function of *frequency* and *temperature*. All presented ImM graphs demonstrate the formation of distinct relaxation peaks in all NCs. Thus, these peaks represent cases where the applied alternating electric field *frequency* matches the dipole reorientation or charge carrier hopping *frequency*. In all studied examples, it was observed that the relaxation peaks shifted to higher *frequencies* as the *temperature* increased, confirming that the processes are thermally activated. Thus, the charge carriers gain more energy with *temperature*, enabling them to hop faster and respond to high-*frequency* fields. In addition, it was stated that the relaxation behavior is mainly due to $Fe^{2+} \leftrightarrow Fe^{3+}$ electron hopping and Maxwell–Wagner type polarization occurring at the core–shell interfaces. While a single and distinct relaxation peak was observed in the undoped example, the relaxation behavior became more complex with increasing $Pr^{3+}$ ion substitution. Specifically, multiple and sharper relaxation peaks were observed for $x = 0.04$ and 0.06 NCs, indicating the emergence of new relaxation environments. These changes were attributed to lattice distortion, alterations in cation distribution, and the formation of new energy barriers for electron hopping. At higher substitution levels ($x = 0.08$ and 0.10), the relaxation peaks were found to broaden and, in some cases, merge. In conclusion, it was shown that $Pr^{3+}$ ion substitution significantly modifies the dielectric relaxation processes and charge-carrying dynamics of ferrite NPs [14].

## 3.8 Nyquist analysis of electric modulus

Nyquist modulus plots (ImM–ReM) of the NFO/$MnPr_xFe_{2-x}O_4$ ($x \leq 0.10$) NCs indicated in Fig. 12 were evaluated to analyze the dielectric relaxation processes. As can be seen from each plot of the figures, one or more semicircular structures were observed in all NCs, but these semicircles were determined to be non-ideal and depressed. Therefore, this type of situation indicates non-Debye type relaxation behavior and a wide relaxation time distribution. Structural and compositional heterogeneity in ferrite systems has

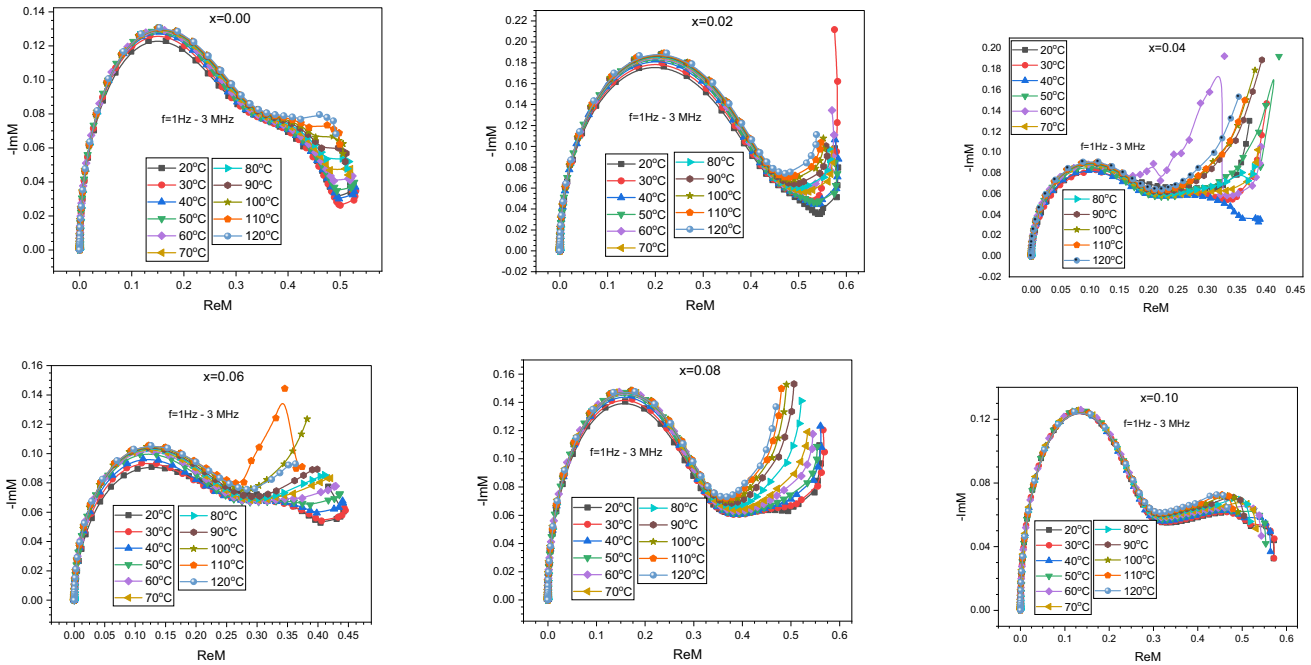


**Fig. 12** Nyquist plot of the imaginary to real modulus of NFO/$MnPr_xFe_{2-x}O_4$ ($x \leq 0.10$) NCs

been shown as the main reason for this behavior. The increase in semicircle dimensions with increasing *temperature* is quite remarkable, confirming that the relaxation processes are thermally activated. The fact that the $Pr^{3+}$ion substitution ratio has a significant effect on the number and shape of semicircles is an important difference. It should be emphasized that a single, large semicircle was observed for $x = 0.00$, 0.02, 0.08, and 0.10, which can be explained by a single-dominant relaxation mechanism or a combination of processes with similar relaxation times. In contrast, two distinct and overlapping semicircles formed at $x = 0.04$, while a weaker similar behavior was observed at $x = 0.06$. It is well known that the semicircle in the high-*frequency* region represents intragranular relaxation, while the semicircle in the low-*frequency* region represents grain boundary or core–shell interface relaxation. In conclusion, the results show that $Pr^{3+}$ion substitution modifies the internal electrical heterogeneity of ferrite NPs and leads to the formation of different relaxation mechanisms [14]. In particular, it was exhibited that the core and interface regions are electrically distinctly separated at the substitution ratio of $x = 0.04$.

## 3.9 Real impedance (ReZ) analysis

The real impedance (ReZ) behavior of NFO/$MnPr_xFe_{2-x}O_4$ ($x \leq 0.10$) NCs exhibited in Fig. 13 was investigated as a *frequency* and *temperature* dependence. As can be seen from each plot, a high impedance plateau at low *frequencies* and a sharp drop at high *frequencies* were observed in all NCs. Therefore, this behavior indicates that grain boundaries at low *frequencies* and intra-grain particles at high *frequencies* are the dominant contributors to the electrical response. Thus, the downward shift of all ReZ spectra as the *Temperature* increases confirms the negative *temperature* coefficient resistivity (NTCR) behavior typically observed in ferrites. This situation is explained by the decrease in the resistivity component due to the ease of $Fe^{2+} \leftrightarrow Fe^{3+}$ electron hopping with increasing *temperature*. When evaluated together with the dielectric relaxation results, it can be understood that the relaxation peaks shift to higher *frequencies* with increasing *temperature* and that this originates from the same thermally activated hopping mechanism. Interestingly, at 20 °C, the low-*frequency dc* resistance was approximately 40 MΩ for $x = 0.00$, decreasing to approximately 7 MΩ at $x = 0.06$, and then rising again to approximately 60 MΩ at $x = 0.10$. Therefore, this intriguing result demonstrates that moderate $Pr^{3+}$ ion substitution level facilitates electron hopping by optimizing the $Fe^{2+}/Fe^{3+}$ ratio. At higher substitution levels, it was determined that $Pr^{3+}$ ions with large ionic radii create lattice strain and grain boundary irregularities. Furthermore, these structural irregularities reduce

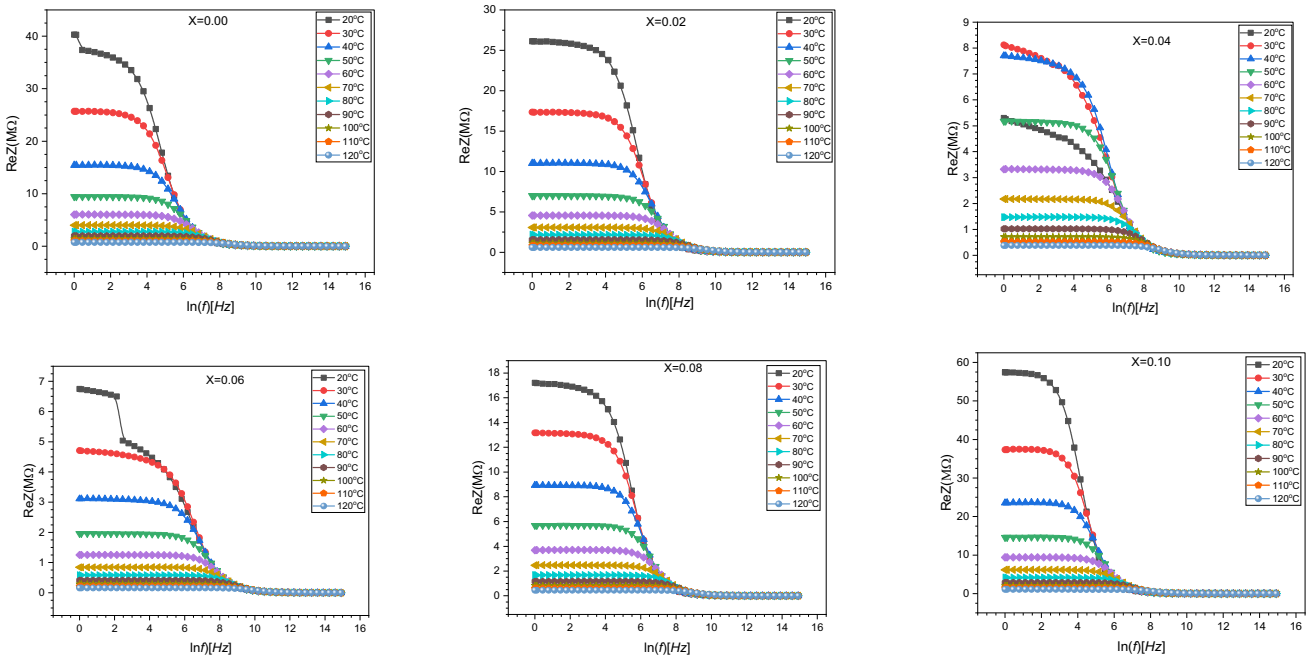


**Fig. 13** Real impedance of NFO/$MnPr_xFe_{2-x}O_4$ ($x \leq 0.10$) NCs

charge carrier mobility, thereby increasing resistance [17, 18, 22]. In conclusion, it has been shown that $Pr^{3+}$ ion substitution can precisely tune the electrical properties of ferrites by influencing both charge carrier dynamics and microstructure.

## 3.10 Imaginary impedance (ImZ) analysis

The imaginary impedance (ImZ) spectra of NFO/$MnPr_xFe_{2-x}O_4$ ($x \leq 0.10$) NCs demonstrated in Fig. 14 were evaluated to investigate the dielectric relaxation and energy loss mechanisms. It is evident that broad and distinct relaxation peaks were observed in all NCs. Subsequently, the *frequency* at which these peaks occur ($f_{max}$) represents the relaxation *frequency* at which energy loss is maximum, and the relaxation time is calculated using the relationship $\tau = 1/(2\pi f_{max})$. It was determined that the relaxation peaks shifted to higher *frequencies* as the *temperature* increased, indicating that the processes are thermally activated. It is worth noting that the faster motion of charge carriers at high *temperatures* allows them to respond to higher *frequency* electric fields. At the same time, the decrease in peak heights with *temperature* confirms the semiconductor character of the system and its negative *temperature* coefficient resistive behavior. Accordingly, the effect of $Pr^{3+}$ ion substitution on the relaxation processes is clearly seen from the peak heights. Consequently, the decrease in peak heights from $x = 0.00$ to 0.06 indicates an increase in conductivity and a decrease in impedance. The re-emergence of peaks at $x = 0.08$ and 0.10 NCs reveals that structural irregularities at high $Pr^{3+}$ ion substitution levels reduce conductivity. The lowest impedance and highest conductivity were obtained at approximately $x = 0.06$ NC. It was noted that relaxation processes are primarily controlled by grain boundaries and core–shell interfaces. The results demonstrate that $Pr^{3+}$ ion substitution is an effective method for optimizing the electrical and dielectric properties of ferrite NPs.

Overall, imaginary impedance analysis confirmed the presence of a strong, thermally activated relaxation process in the NCs. This relaxation is most likely dominated by the effects of grain boundaries or the core–shell interface acting as barriers to charge transport. Accordingly, the results strongly support the findings from the real impedance (ReZ) and electric modulus (ReM) plots, showing that the electrical properties of these NCs can be systematically controlled by the Pr substitution level [17, 18, 22].

## 3.11 Cole–Cole analysis of complex impedance

The Cole–Cole impedance plots of NFO/$MnPr_xFe_{2-x}O_4$ ($x \leq 0.10$) NCs depicted in Fig. 15 were analyzed to investigate the electrical conduction mechanisms and

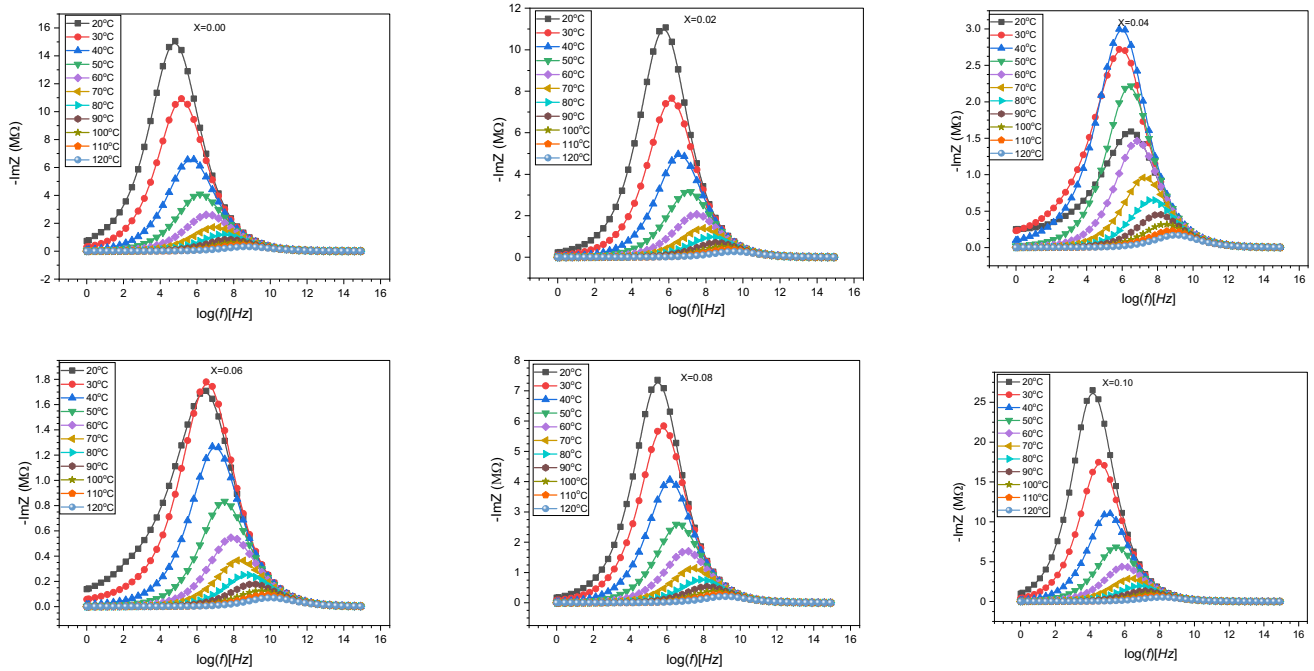


**Fig. 14** Imaginary impedance of NFO/$MnPr_xFe_{2-x}O_4$ ($x \leq 0.10$) NCs

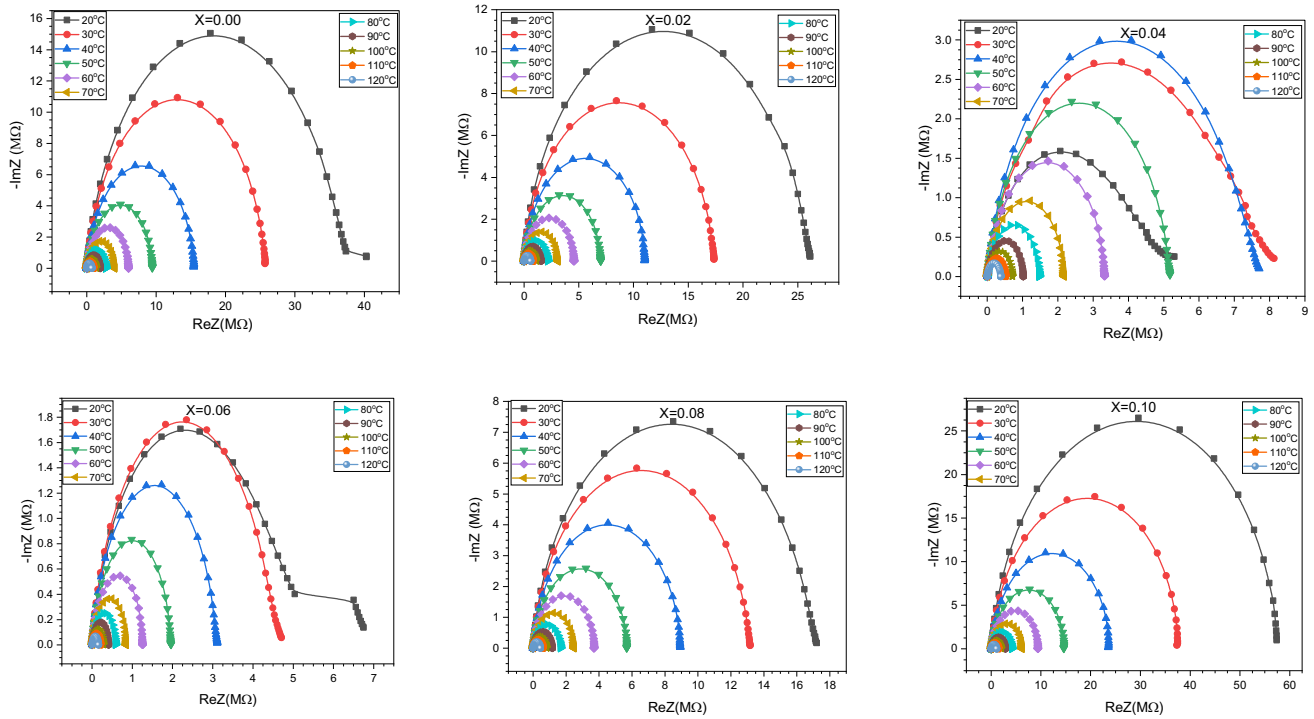


**Fig. 15** Nyquist plot of the imaginary to real impedance of NFO/$MnPr_xFe_{2-x}O_4$ ($x \leq 0.10$) NCs

microstructural contributions of ferrites. Nyquist plots were used to plot –ImZ versus ReZ values, and the contributions of different electroactive regions were evaluated. Wide and depressed semicircle structures were observed in all NCs, revealing non-Debye relaxation behavior and distributed relaxation times. It was clearly stated that high-*frequency* semicircles represent intragranular resistance, while low-*frequency* semicircles represent grain boundary resistance. It was determined that increasing the $Pr^{3+}$ ion substitution ratio at constant *temperature* increased the semicircle diameters, indicating an increase in total resistance. It was apparently stated that $Pr^{3+}$ ions with large ionic radii caused lattice distortion, altered cation distribution, and hindered $Fe^{2+} \leftrightarrow Fe^{3+}$ electron hopping. Therefore, it was concluded that $Pr^{3+}$ ion substitution ratio specifically restricts charge transport at grain boundaries. In contrast, the decrease in semicircle diameters with increasing *temperature* at a constant substitution ratio confirms the negative *Temperature* coefficient resistance behavior. Increasing *temperature* facilitated the small polaron hopping mechanism, increasing charge carrier mobility and reducing resistance. Consequently, it was clearly presented that $Pr^{3+}$ ion substitution significantly changes the microstructure, relaxation processes, and conduction properties of ferrite NPs. The findings demonstrate that optimized ferrite materials for high-*frequency* electronics, sensors, and electromagnetic applications can be developed through controlled substitution [17, 19].

## 4 Conclusions

In this study, NFO/$MnPr_xFe_{2-x}O_4$ ($x \leq 0.10$) NCs were synthesized in one-pot sol–gel auto combustion approach. The XRD and EDX analyses proved cubic crystal structure and the purity of all products (including NPs and NCs). The cubic morphology of all products has been verified by SEM and TEM techniques. The impedance analysis of NFO/$MnPr_xFe_{2-x}O_4$ ($x \leq 0.10$) NCs demonstrated that the materials exhibit a negative *temperature* coefficient of resistance, consistent with a thermally activated conduction mechanism typical of spinel ferrites. The total *dc* resistance, primarily governed by grain boundary effects, was found to be minimized at a substitution level of $x = 0.06$, indicating that this NC possesses the highest overall conductivity. Furthermore, complementary analysis using the electric modulus formalism, which is sensitive to bulk phenomena, provided deeper insight into the internal dielectric structure. A unique dielectric signature was observed for the $x = 0.04$ NC, which displayed multiple relaxation peaks and two resolved semicircles in the modulus spectrum. This signifies the presence of at least two distinct relaxation mechanisms within the grains, a feature not observed in the other NCs. The central conclusion of this work is the elucidation of the differential role of the Pr dopant on the electrical properties of the grains and grain boundaries. The optimization of *dc* conductivity ($x = 0.06$) is governed by the modulation of grain boundary characteristics, whereas the emergence of a complex bulk dielectric response ($x = 0.04$) is a grain-centric phenomenon. These findings are significant as they demonstrate that the overall *dc* conductivity and the internal dielectric relaxation behavior can be independently tuned by careful control of dopant concentration. This provides a valuable framework for the rational design of ferrite-based core–shell nanostructures for specific electronic applications, such as high-*frequency* inductors, electromagnetic interference (EMI) shielding, or dielectric resonators.

## Acknowledgements

Acknowledgements The authors acknowledge the funding obtained from the Research, Development, and Innovation Authority (RDIA), Saudi Arabia, Riyadh, Reactivating & Rebuilding of Existing Labs Initiative, number 12959-iau-2023-iau-R-3-1-SE, supporting the generation of TEM images. Prof. A. Baykal acknowledges Istanbul Aydin University Project Support Center with the project number of IAU BAP 2026-3.

## Author contributions

M.A. Almessiere contributed toward conceptualization, methodology, data curation, writing—original draft, and funding acquisition. A. Baykal contributed toward supervision, conceptualization, methodology, writing—reviewing and editing, data curation, and funding acquisition. B. Ünal contributed toward formal analysis, investigation, and writing—original draft preparation. Y. Slimani contributed toward formal analysis, investigation, writing—original draft, and writing—review & editing. A. Demir Korkmaz contributed toward formal analysis and investigation.

## Funding

The authors acknowledge the funding obtained from the Research, Development, and Innovation Authority (RDIA), Saudi Arabia, Riyadh, Reactivating & Rebuilding of Existing Labs Initiative, number 12959-iau-2023-iau-R-3-1-SE, supporting the generation of TEM images. Prof. A. Baykal acknowledges Istanbul Aydin University Project Support Center with the project number of IAU BAP 2026–3.

## Data availability

No datasets were generated or analysed during the current study.

## Declarations

**Competing interests** The authors declare no competing interests.

**Ethical approval** Not applicable.

## References

1. K. Biswas, R. Kameshwaran, L. Inbathamizh, N.F. Islam, H. Sarm, Spinel ferrite nanoparticles: multifaceted applications and future perspectives in biomedical and environmental sciences. Next Res. **5**, 101364 (2026)
2. D.H.K. Reddy, Y. Sang Yun, Spinel ferrite magnetic adsorbents: alternative future materials for water purification? Coord. Chem. Rev. **315**, 90 (2016)
3. O.D. Dastjerdi, H. Shokrollahi, S. Mirshekari, A review of synthesis, characterization, and magnetic properties of soft spinel ferrites. Inorg. Chem. Commun. **153**, 110797 (2023)
4. T.T.V. Nga, N.T. Lan, T.T. Loan, H. Ha, Structure and magnetic properties of $SrFe_{12}O_{19}/CoFe_2O_4$ nanocomposite ferrite. VNU J. Sci.: Math. Phys. **35**(2), 32 (2019)
5. K. Dhabekar, K.M. Kant, Soft/hard ferrite nanocomposites: evaluation of temperature dependent dielectric properties. Phys. B **627**, 413581 (2022)
6. A. Rahman, R. Jayaganthan, Study of $CoFe_2O_4/NiFe_2O_4$ nanocomposite ferrite film. Surf. Eng. **33**, 810 (2017)
7. C. Feng, X. Liu, S.W. Or, S. Ho, Exchange coupling and microwave absorption in core/shell-structured hard/soft ferrite-based $CoFe_2O_4/NiFe_2O_4$ nanocapsules. AIP Adv. **7**, 056403 (2017)
8. Y. Slimani, M.A. Almessiere, A. Baykal, M.A. Gondal, N. Tashkandi, Impact of sonication time on the structural and magnetic features of $CoFe_2O_4/Ni_{0.8}Cu_{0.1}Zn_{0.1}Fe_2O_4$ hard-soft nanocomposites. J. Alloys Compd. **923**, 166347 (2022)
9. L. Wang, C. Yang, L. Zhang, Y. Hu, J. Lia, S. Xua, H. Li, The exchange coupling interaction in $CoFe_2O_4/Fe_3O_4$ hard and soft magnetic nanocomposites. Vacuum **181**, 109751 (2020)
10. H. Jalili, B. Aslibeiki, A. Hajalilou, O. Musalu, L.P. Ferreira, M.M. Cruz, Bimagnetic hard/soft and soft/hard ferrite nanocomposites: structural, magnetic and hyperthermia properties. Ceram. Int. **48**, 4886 (2022)
11. T.T.V. Nga, C.M. Hung, T.T.H. Duong, Core/shell $CoFe_2O_4/Fe_3O_4$ nanoparticles: effects of hard/soft magnetic weight fraction on structure, particle size and magnetic properties. Commun. Phys. **33**(1), 41 (2023)
12. M.A. Almessiere, S.E. Shirsath, A. Baykal, Y. Slimani, Electrodynamic and electrical/dielectric features of $Co_{0.5}Ni_{0.5}Sc_{0.04}In_{0.04}Fe_{1.92}O_4@MFe_2O_4$ (M = Mg, Cu, Zn, Mn) soft-soft nanocomposite. J. Sol-Gel Sci. Technol. **116**, 226 (2025)
13. M.M.N. Ansari, S. Khan, Structural, electrical and optical properties of sol-gel synthesized cobalt substituted $MnFe_2O_4$ nanoparticles. Physica B **520**, 21 (2017)
14. H.M.T. Farid, I. Ahmad, I. Ali, S.M. Ramay, A. Mahmood, G. Murtaza, Dielectric and impedance study of praseodymium substituted Mg-based spinel ferrites. J. Magn. Magn. Mater. **434**, 143 (2017)
15. C. Murugesan, K. Ugendar, L. Okrasa, J. Shen, G. Chandrasekaran, Zinc substitution effect on the structural, spectroscopic and electrical properties of nanocrystalline $MnFe_2O_4$ spinel ferrite. Ceram. Int. **47**, 1672 (2021)
16. B. Ünal, M.A. Almessiere, I.A. Auwal, Y. Slimani, A. Baykal, The role of $Pr^{3+}$, $Pr^{3+}$-$Y^{3+}$ and $Pr^{3+}$-$Y^{3+}$-$Dy^{3+}$ ions substitutions on the electrical and dielectric properties of NiCo nanospinel ferrites. J. Alloys Compd. **944**, 169096 (2023)
17. D.L. Sekulic, Z.Z. Lazarevic, M.V. Sataric, C.D. Jovalekic, N.Z. Romcevic, Temperature-dependent complex impedance, electrical conductivity and dielectric studies of $MFe_2O_4$ (M = Mn, Ni, Zn) ferrites prepared by sintering of mechanochemical synthesized nanopowders. J. Mater. Sci. Mater. Electron. **26**, 1291 (2015)
18. C. Behera, R.N.P. Choudhary, Electrical and multiferroic characteristics of PVDF-$MnFe_2O_4$ nanocomposites. J. Alloys Compd. **727**, 851 (2017)
19. D.L. Sekulić, Z.Ž Lazarević, Č Jovalekić, A. Rečnik, M. Romčević, B. Hadžić, N.Ž Romčević, The comparative

study of the structural and the electrical properties of the nano spinel ferrites prepared by the soft mechanochemical synthesis. Sci. Sinter. **46**, 235 (2014)

20. B. Ünal, M.A. Almessiere, A. Baykal, Y. Slimani, M.A. Gondal, N. Kian-Pour, S.E. Shirsath, A. Manikandan, U. Baig, Ceram. Int. **50**, 30670–30682 (2024)
21. S.F. Mansour, O.M. Hemeda, M.A. Abdo, W.A. Nada, Improvement on the magnetic and dielectric behavior of hard/soft ferrite nanocomposites. J. Mol. Struct. **1152**, 207 (2018)
22. Z.A. Gilani, M. Khalid, A. Ahmed, A.K. Khan, M.R. Khan, F.A. Sheikh, N. Ahmad, R. Busquets, Structural, dielectric, impedance and electric modulus properties of praseodymium-substituted $BaPr_xFe_{12-x}O_{19}$ nanoparticles synthesized via sol–gel method. Appl. Phys. A **128**, 762 (2022)

**Publisher's Note** Springer Nature remains neutral with regard to jurisdictional claims in published maps and institutional affiliations.

Springer Nature or its licensor (e.g. a society or other partner) holds exclusive rights to this article under a publishing agreement with the author(s) or other rightsholder(s); author self-archiving of the accepted manuscript version of this article is solely governed by the terms of such publishing agreement and applicable law.